



HAL
open science

A significant doubling of rockfall rates since the Little Ice Age in the Mont-Blanc massif, inferred from ^{10}Be concentrations and rockfall inventories.

Léa Courtial-Manent, Jean-Louis Mugnier, Ludovic Ravel, Julien Carcaillet, Philip Deline, Jean-François Buoncristiani

► To cite this version:

Léa Courtial-Manent, Jean-Louis Mugnier, Ludovic Ravel, Julien Carcaillet, Philip Deline, et al.. A significant doubling of rockfall rates since the Little Ice Age in the Mont-Blanc massif, inferred from ^{10}Be concentrations and rockfall inventories.. Earth and Planetary Science Letters, 2025, 651, pp.119142. 10.1016/j.epsl.2024.119142 . hal-04873375

HAL Id: hal-04873375

<https://u-bourgogne.hal.science/hal-04873375v1>

Submitted on 9 Jan 2025

HAL is a multi-disciplinary open access archive for the deposit and dissemination of scientific research documents, whether they are published or not. The documents may come from teaching and research institutions in France or abroad, or from public or private research centers.

L'archive ouverte pluridisciplinaire **HAL**, est destinée au dépôt et à la diffusion de documents scientifiques de niveau recherche, publiés ou non, émanant des établissements d'enseignement et de recherche français ou étrangers, des laboratoires publics ou privés.



Distributed under a Creative Commons Attribution 4.0 International License



A significant doubling of rockfall rates since the Little Ice Age in the Mont-Blanc massif, inferred from ^{10}Be concentrations and rockfall inventories

Léa Courtial-Manent ^{a,b,*}, Jean-Louis Mugnier ^a, Ludovic Ravel ^b, Julien Carcaillet ^a, Philip Deline ^b, Jean-François Buoncristiani ^c

^a ISTerre, Université Grenoble Alpes, Université Savoie Mont Blanc, CNRS, IRD, Univ. G. Eiffel, Grenoble, France

^b EDYTEM, Université Savoie Mont Blanc, CNRS, UMR 5204, Le Bourget-du-Lac, France

^c Biogéosciences, UMR 6282, CNRS/Université Bourgogne Franche-Comté, Dijon, France

ABSTRACT

By combining cosmogenic nuclide data and rockfall inventories, we have employed a rigorous methodology to focus on long-term erosion trends and the increase in rockfall in the Mont-Blanc massif (European Alps) over the last century. To do this, we used mathematical formulations based on power law integration, which enabled us to identify the complex links between rockfall distribution and erosion rates. Our approach was applied to the Mer de Glace basin (Mont-Blanc massif), where we combined analyses of ^{10}Be concentration in the supraglacial load (based on 8 samples) with Terrestrial Laser Scanning (TLS) data capturing 123 rockfalls ranging from 1 to 566 m³, as well as direct observations of 71 rockfalls ranging from 100 to 20,000 m³. Within the overlapping volume range of both inventories, power law fitting yields a common exponent (*b*-value) of 0.75 ± 0.18 . However, the TLS-derived rockfall rate (\bar{a} in m².yr⁻¹) is approximately 5 times higher than that derived from the observation-based inventory. This difference is probably linked to the current intense permafrost degradation affecting scanned rockwalls at altitudes below 3800 m a.s.l. The 20,000 m³ rockfall documented by the network of observers has a statistical return time estimated at <6 years, which suggests that larger or more significant rockfalls will occur in the future. Based on a two-segment power law, the erosion rate is estimated at > 4.1 mm.yr⁻¹ for the period 2006–2011.

According to our study of glacial dynamics, the supraglacial clasts sampled aggregate 800 rockfalls greater than 1 m³ that occurred diachronically between 1845 and 1987 but whose cumulative total corresponds to <7 years of present rockwall erosion rate in the upper Mer de Glace basin. The mean ^{10}Be concentration of the 8 supraglacial samples is $2.7 \pm 1.3 \cdot 10^4$ at.g⁻¹ and was obtained when exposing rock faces subjected to erosion of $<1.2 \pm 1$ mm.yr⁻¹. The erosion rate would, therefore, have significantly increased between the Little Ice Age (maximum 2.2 mm.yr⁻¹ from ^{10}Be result) and the beginning of the 21st century (minimum 4.1 mm.yr⁻¹ for 2003–2011 surveys). These erosion rates do not consider past volume rockfalls greater than those observed recently and are minimal erosion rate estimates. Nevertheless, they highlight the increase in mass movement hazards linked to global warming *via* permafrost degradation in high-altitude rockwalls.

1. Introduction

Since the end of the Little Ice Age (~1855), human activity has drastically been affected by the sensitivity of high-mountain landscapes to climate, and climate change impacts have become a matter of growing global concern in Alpine areas (Haerberli and Beniston, 1998; Adler et al., 2019). The European Alps, a densely populated region, face rising mass movement risks with climate change, endangering communities, infrastructure, and the tourism economy (Beniston, 2003; Gobiet et al., 2014) as the cryosphere is degrading and erosion processes are changing (Ballantyne, 2002; Cossart et al., 2008; Biskaborn et al., 2019; Hartmeyer et al., 2020).

Past rockfall inventories provide a base for estimating rockfall

hazards (Dussaige et al., 2003). However, what areas and periods are inventories representative of? Is there really a change in rockfall activity? In this paper, we use a method that considers an independent estimate of long-term erosion, enabling a better assessment of rockfall hazard. Long-term erosion, on the scale of river catchments, is classically estimated using methods based on the concentration of cosmogenic nuclides in sediments (von Blanckenburg, 2006). This approach has also been adapted to the rockwalls surrounding glaciers (Ward and Anderson, 2011; Sarr et al., 2019; Scherler and Egholm, 2020; Orr et al., 2021; Wetterauer et al., 2022; Wetterauer and Scherler, 2023) as glacial transport amalgamates rockfalls deposited on them and the supraglacial load is composed of rockfalls from various rockwalls in the upper part of the supply basin.

* Corresponding author.

E-mail address: lea.courtial-manent@univ-smb.fr (L. Courtial-Manent).

<https://doi.org/10.1016/j.epsl.2024.119142>

Received 29 May 2024; Received in revised form 12 November 2024; Accepted 25 November 2024

Available online 5 December 2024

0012-821X/© 2024 The Author(s). Published by Elsevier B.V. This is an open access article under the CC BY license (<http://creativecommons.org/licenses/by/4.0/>).

It is suggested that a major factor in rockwall destabilization in high-Alpine areas is permafrost degradation due to global warming (Gruber and Haeblerli, 2007; Biskaborn et al., 2019). This is linked to a deepening of the active layer subject to annual freeze/thaw cycles and general warming at greater depths (Krautblatter et al., 2013). Permafrost degradation would be particularly intense at elevations below 3800 m a.s.l. in the Mont Blanc massif (MBM) (Magnin et al., 2017; Courtial-Manent et al., 2024).

This study is a comprehensive approach to rockwall erosion trends by integrating three methods: collecting rockfall inventories (Terrestrial Laser Scanning (TLS) and a network of observers), analyzing them with a power law (Graber and Santi, 2022), and estimating erosion by measuring cosmogenic nuclides concentration on glacier-transported clasts. The upper basin of the Mer de Glace (UMdG hereafter), located between 2950 and 4200 m a.s.l. in the MBM, was chosen as the study area for applying all three methods. This location was selected due to its exceptional suitability for this research, owing to the abundance of existing studies across various disciplines in terms of glacier dynamics (from Vallot, 1900 to Peyaud et al., 2020), dating old rockfall scars (Gallach et al., 2020), rockfall analysis (Ravanel et al., 2011; Deline et al., 2015; Courtial-Manent et al., 2024), or temperature-related destabilization processes (Legay et al., 2021).

This paper presents new cosmogenic nuclides data from amalgamations of supraglacial clasts from the UMdG, as well as 2009 to 2011 rockfall observations that, complemented by the Ravanel et al. works (2010; 2011; 2017), furnish a 2003 to 2011 inventory in the UMdG (Fig. 1A). For this period, being the beginning of rigorous rockfall observations in the MBM, the broad inventory is considered reasonably complete (Rabatel et al., 2008; Ravanel and Deline, 2013). The

contributions of these combined approaches are discussed, in particular, to clarify the notion of “long-term erosion” and give a minimum estimate of the increase of the rockfall rate since one century.

2. Setting

The MBM is the highest range in the European Alps, reaching 4806 m a.s.l. (Fig. 1A). It is a heavily glaciated massif, with 145 km² covered by glaciers (Kaushik et al., 2022). Its central part is made up of homogeneous granite (Bussy et al., 1989). On the southern slopes of MBM, large rock avalanches (volume > 10⁶ m³ and thickness-50 m) have been evidenced (Deline et al., 2015).

After 2003, rockfall occurrence and volume have been estimated using three methods: diachronic TLS surveys (Rabatel et al., 2008; Ravanel et al., 2011), recognition of rockfall deposits on satellite images (Ravanel et al., 2017), and surveys carried out with a network of observers (Ravanel et al., 2010, 2017). These two last methods allowed us to record >313 rockfalls in the central part of MBM, in the range of 100 m³ to 50,000 m³ (Ravanel et al., 2010), and the cumulative frequencies of rockfall events show a power law model with an exponent of 0.77 ± 0.04 (Ravanel et al., 2017). TLS surveys show that the annual volume of rockfalls from specific rockwalls has increased 8-fold over the 21st century due to global warming (Courtial-Manent et al., 2024).

Initial estimates of the long-term erosion rates of rockwalls were based on the cumulative effect of rockfalls estimated from the concentration of ¹⁰Be in clasts transported near glaciers (Guillon et al., 2015). Results vary by one order of magnitude, from 0.38 ± 0.16 mm.yr⁻¹ for the highest north face of the Mont Blanc summit to 2.16 ± 0.24 mm.yr⁻¹ in the west face of Aiguille du Midi (Sarr et al., 2019).

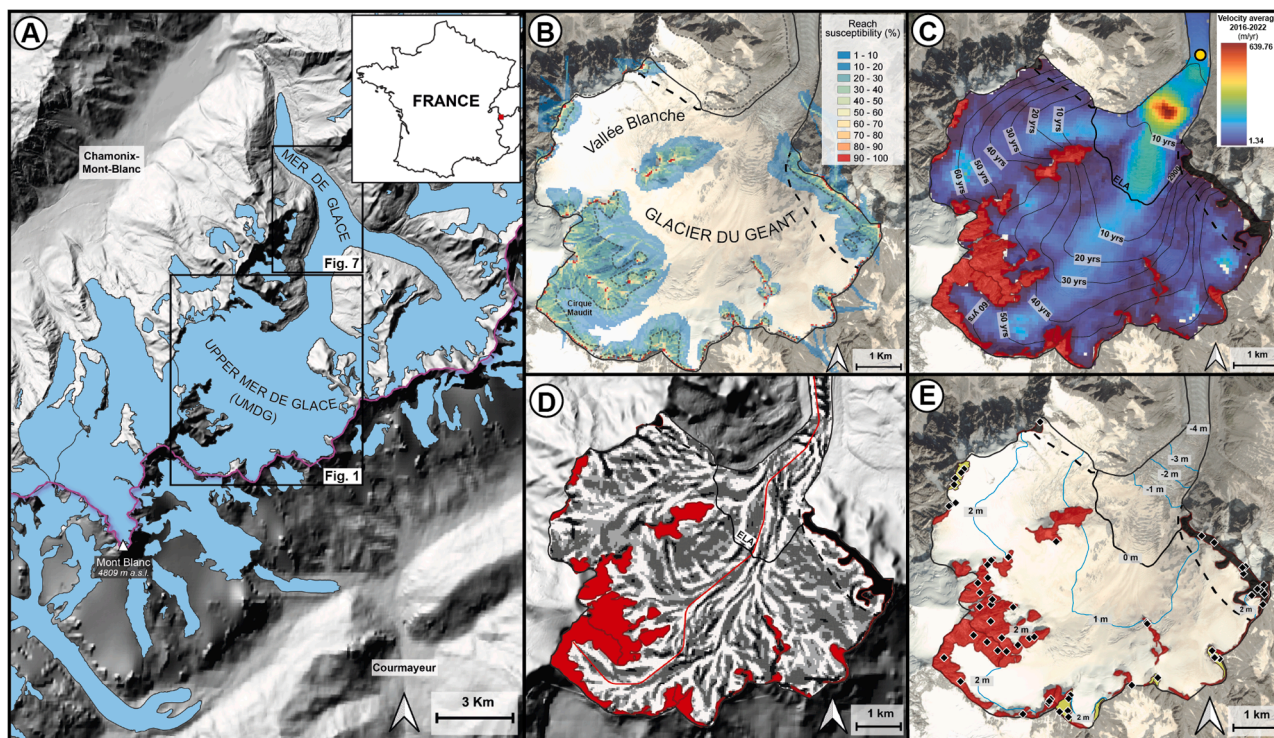


Fig. 1. (A) The Upper Mer de Glace (UMdG) study area. Black rectangles: this figure and Fig. 7. (B) Rockfall reach susceptibility. Scale in % according to Cathala et al. (2024). Dotted line: boundary between glacier and rockwall. (C) Glacier velocities (Rabatel et al., 2023). Black lines: isotransport time relative to the ELA considered at 2900 m a.s.l. in 2005–2008; yellow point: start of the Forbes band count of Fig. 7. (D) Superglacial index (light-grey color) following the glacier surface gradient outlining the glacier flow. Red line: Fig. 5a cross-section. (E) Contributing rockwalls to the supraglacial load (red color: surely; heavy grey: possibly) and TLS scanned rockwalls (yellow zones, see Ravanel et al., 2011; Supplementary Material S1). Black diamonds: inventoried rockfalls (Ravanel et al., 2010, 2017; Supplementary Material S2); blue lines: snow isoaccumulation (positive) or ablation value (negative) (2005–2008 period, adapted from *Glacioclim*). The location of ¹⁰Be samples, Forbes bands, and rockfalls are in a kmz-file in Supplementary material.

We focus our work on the UMdG (Fig. 1), with the largest glacier in the MBM (28 km²) located between 4213 and 1520 m a.s.l. (Kargel et al., 2014). Climate change over the 20th century led to an increase of the equilibrium line (ELA) from 2750 to 2900 m a.s.l. and a decrease in glacier velocity (Vincent et al., 2017). In the lower part of the MdG, a decrease of over 100 m.yr⁻¹ (i.e. -66 %) was observed between 1890 and 1950 (Liboutry and Reynaud, 1981), based on counts of the annual cycle of white and grey ice bands (Forbes, 1843).

The UMdG rockwalls feed supraglacial moraines. In the area below the equilibrium line, erosion of the Holocene lateral moraines supplies debris to MdG margins (Le Roy et al., 2015), and rockfalls from lower MdG slopes are very unlikely to go farther than the glacier margins, as shown by rockfall propagation models (Fig. 1B, Cathala et al., 2024).

3. Methods

3.1. Distribution of the rockfall volumes and erosion rate

3.1.1. Rockfall inventories

Reiterations of topographic measurements by TLS (Fig. 2A) enable an inventory of rockfalls and the associated volumes for periods close to the year (Supplementary Material S1). Given the accuracy of the TLS given by the constructor (7 10⁻⁵, i.e., 7 mm at a distance of 100 m (Teledyne Geospatial Optech, 2024)), many blocks < 1 m³ can be identified (Guerin et al., 2020). However, to ensure that the distribution of rockfall volumes is not affected by a bias linked to incomplete data acquisition, only rockfalls exceeding a minimum volume (V_{min}) of 1 m³ have been included in the inventory.

Thanks to a systematic procedure to describe rockfalls in the MBM (Fig. 2B), mainly by a network of mountain professionals (Ravanel and Deline, 2013), an inventory of rockfalls > 100 m³ was obtained (Ravanel et al., 2010, 2017) (Supplementary Material S2). Satellite images at a 2.5 m resolution have also been used to map the rockfall deposits of the hot summer of 2003, but the uncertainty in the volume estimation can reach 40 % (Ravanel et al., 2017).

3.1.2. Rockfall volume distribution and power law

The volumes of rockfall inventories are classically described by their rockfall volumes' cumulative distribution of magnitude (CDM) (Graber and Santi, 2022), and can be approximated by a power law (Hantz et al., 2021). Power laws describe many series of events in Earth sciences where any observed magnitude distribution is regarded as an estimate of the mean value of a random variable (Aki, 1965). Assuming that the power law reflects scale-invariant physical processes (Turcotte, 1986; Malamud and Turcotte, 2006), cumulated distributions obtained for different periods by different observation methods would fit a unique power law. The power law is therefore used to merge data from different sources and time periods, facilitating the creation of regional inventories

that integrate observations from different acquisition procedures and areas (Hantz et al., 2003).

The comparison of different CDM requires approximating them with specific rockfall frequency functions (SRFF) defined by Eq. (1):

$$fs(V) = a/(S.T)V^{-b} \quad \text{or} \quad fs(V) = \bar{a}V^{-b} \quad (1)$$

where $fs(V)$ is the frequency of rockfalls with volume (V) > 1 m³ per year and per unit rockwall area (m²), a is the number of rockfalls, S is the projection of the oblique surface area of a rock face on the horizontal, T the observation time, b is the power law exponent, and \bar{a} is the annualized frequency of rockfalls > 1 m³ per unit of rockwall ($\bar{a} = a/(S*T)$) (Hantz et al., 2021).

3.1.3. Rockfall erosion rate and power law

In this paper, all the erosion rates are defined normal to the rockwall. The mean observed erosion rate ϵ_{ob} is the sum of the rockfall volumes observed ($V_{t_{ob}}$) in the range between the minimum (V_{min}) and maximum (V_{max}) values for a period (T) and a rockwall surface area (S).

$$\epsilon_{ob} = V_{t_{ob}}/(S.T) \quad (2)$$

The mathematic integration of the power law is another way to determine the erosion rate. The total eroded volume V_{t_p} due to rockfalls of volumes comprised between v_1 and v_2 is (Hantz et al., 2003):

$$V_{t_p} = \int_{v_2}^{v_1} aV^{-b}dv \quad \text{or} \quad V_{t_p} = \frac{a}{(1-b)}(v_2^{(1-b)} - v_1^{(1-b)}) \quad (3)$$

In this work, Eq. (2) and Eq. (3) are combined (details in Supplementary Material S3.1) to calculate an erosion value (ϵ_{pl}) that depends on the maximal volume V_{mp} through a power law relation:

$$\epsilon_{pl} = \frac{a}{(1-b)S.T} V_{mp}^{(1-b)} \quad \text{or} \quad \epsilon_{pl} = \frac{\bar{a}}{(1-b)} V_{mp}^{(1-b)} \quad (4)$$

3.1.4. The application domain of the power law

The fit of the SRFF parameters was performed only in the range between the cutoff values V_{Cmi} and V_{Cma} (Fig. 3).

For volumes lower than V_{Cmi} , the cumulative number of rockfalls observed is usually lower than that calculated by the SRFF power law. This discrepancy can be attributed either to the incompleteness of the inventory linked to the detection threshold of the acquisition (Graber and Santi, 2022) or a change in the processes behind the delimitation of blocks before they fall (Guthrie and Evans, 2004). Various methods can be used to determine the V_{Cmi} value (Schovanec et al., 2021), and we analyze here the influence of V_{Cmi} on the coefficient of determination r^2 , defined as $1-(SSE/(SSE+SSr))$, where SSE is the residual sum of squares and SSr is the regression sum of squares.

For very large rockfalls, the power law may not be suitable (Coles,



Fig. 2. Used methods. (A) Example of TLS survey on the east face of Tour Ronde. (B) Example of a rockfall in the north face of Tour Ronde documented by the network of observers (August 2022, 12×10^3 m³). (C) Sampling of clasts on supraglacial moraines for ¹⁰Be concentration analysis.

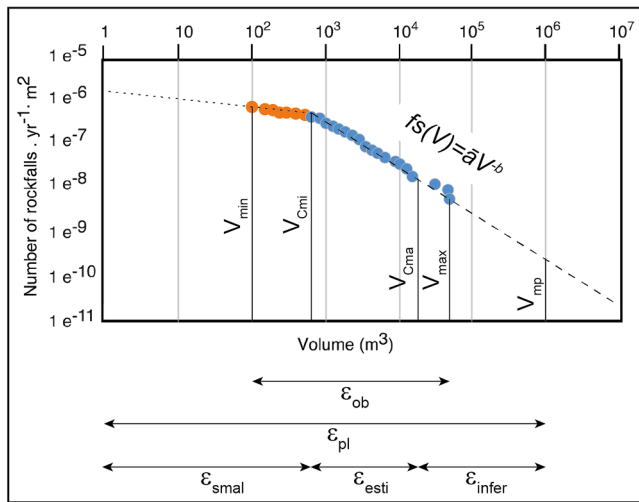


Fig. 3. Definition of cumulative volume distribution, power law, erosion rate estimation, and parameters \bar{a} , b , V_{min} , V_{Cmi} , V_{Cma} , V_{max} , and V_{mp} . Colored dots: rockfalls of a catalog (CDM), dotted and dashed lines: power laws (SRFF). Arrows below: range of volumes used to calculate different erosion rates ϵ_{ob} , ϵ_{pl} , ϵ_{smal} , ϵ_{esti} , ϵ_{infer} .

2004), and the upper cutoff volume V_{Cma} is determined to exclude them from the SRFF fit. The chosen V_{Cma} value excludes rockfalls greater than V_{max} or whose statistic return time is superior to the observation time (See details in Supplementary Material S3.2):

$$[fs(V) = \bar{a} V^{-b}] \text{ if } [V < V_{Cma}] \text{ with } \left[V_{Cma} < V_{max} \text{ or } V_{Cma} < \left(\frac{1}{S \times T \times \bar{a}} \right)^{-\left(\frac{1}{b}\right)} \right] \quad (5)$$

It should be noted that V_{Cma} can be greater than V_{max} , as Poisson's law indicates that the probability of an event occurring during its statistical return time is only 0.63. An iterative calculation is required to estimate both \bar{a} and the upper limit V_{Cma} of the fitting domain.

Extrapolation of the SRFF for rockfalls larger than V_{Cma} or smaller than V_{Cmi} would be possible, but only if the power law reflects scale-invariant physical processes (Turcotte, 1986). These scale-invariant processes can only be envisaged if rock mass, geology, and climate conditions are fairly constant (Graber and Santi, 2022). In the MBM, these conditions are verified. Furthermore, the large inventory covering the surface of the entire massif (references in Sarr et al., 2019) fits with a reliable power law, from the application of Eq. (5), at least up to a regional V_{Cma} of 77,000 m³ (see Supplementary Material S3.2). In contrast, the detailed inventories of the Dru rockwall (MBM) indicate that a power law is reliable at least down to 0.1 m³ (Guerin et al., 2020).

Therefore, we consider using power laws to estimate erosion rates between 0.1 m³ and 77,000 m³ possible. The components of the erosion rate – ϵ_{esti} on the SRFF fitting domain, ϵ_{smal} , and ϵ_{infer} outside of this domain, and ϵ_{pl} the erosion rate for the whole domain (Fig. 3) – are estimated from the integration of the different SRFF power laws to feed the discussion.

3.2. Cosmogenic nuclide concentration in clasts and erosion rate

The transport path of a volume of rock coming from close to a rockwall's surface to a supraglacial location is formed by a succession of several stages: 1) approach to the surface by erosion; 2) incorporation

into a rockfall; 3) deposition on the glacier surface; 4) englacial transport; 5) transport on the glacier surface. ¹⁰Be concentration is mainly acquired during the stages of approach to the surface and transport on the glacier surface, the other stages being either very rapid or protected from cosmic radiation. The duration of rockfall transport depends on the stages of englacial transport and transport on the glacier surface.

3.2.1. Cosmogenic nuclides produced close to the surface

Terrestrial cosmogenic nuclides are produced by the interaction of cosmic rays with rock close to the surface (Dunai, 2010). For the ¹⁰Be, whose radiogenic decay is 1.39 Ma (Chmeleff et al., 2010), radiogenic decay loss is considered negligible (Supplementary Material S4) (Heisinger et al., 1997), and:

$$C_{(z)} = P_0 \cdot T \cdot e^{-\frac{z\rho}{\Lambda}} \quad (6)$$

where $C_{(z)}$ is the concentration at a depth z , P_0 is the ¹⁰Be surface production rate, T is the period of exposition, z is the depth below the surface, ρ is the rock density, and Λ is the absorption mean free path. Several particle sources exist, but only neutrons, which are the most energetic, are considered here with the attenuation length $\Lambda_n = \Lambda / \rho = 0.6$ m (Braucher et al., 2013).

3.2.2. ¹⁰Be concentration and rockfalls

The ¹⁰Be surface concentration of a rockwall is heterogeneous due to the succession of rockfalls (Gallach et al., 2020). This affects the concentration of the rockfall clasts. Nevertheless, Ward and Anderson (2011) numerically modeled the influence of power law exponent value (b) and maximum rockfall thickness (D_{max}) on the average ¹⁰Be con-

centration of a rockfall amalgam. They found that an amalgam of 30 rockfalls approaches the average ¹⁰Be concentration of the rockwall surface with a deviation of <10 % when $b = 0.75$ and $D_{max} = 50$ m. Therefore, the approach used for river sediment fluxes (von Blanckenburg, 2006) is used for supraglacial clasts (Ward and Anderson, 2011; Scherler and Egholm, 2020; Orr et al., 2021; Wetterauer et al., 2022; Wetterauer and Scherler 2023) and leads to:

$$C_0 = \frac{P_{mr} \Lambda_n}{\epsilon_{ml}} \quad (7)$$

where the average concentration (C_0) of the clasts is a function of the average concentration of a surface with an average production rate P_{mr} and eroded at a steady-state rate (ϵ_{ml}) during a period longer than the nuclide integration time ($\Lambda_n / \epsilon_{ml}$) (von Blanckenburg, 2006).

3.2.3. Clast formation

During rockfall, disaggregation generates a fractal distribution of clast size (Turcotte, 1986; Ruiz-Carulla et al., 2017). The sand and gravel fractions on the glacier come from *in situ* rock compartments of different sizes, originating from different *in situ* depths in the rockwall. To increase the likelihood of amalgamating clasts from various rockfalls and various depths in the rockwall compartments, we sampled the sand and gravel fractions (Sarr et al., 2019) that can reach 5 % of the clast volume (Godon et al., 2013). This choice is supported by no apparent dependency of ¹⁰Be concentration with size fractions in supraglacial sediment (Wetterauer et al., 2022), contrary to fluvial sediment provided by landslides (Puchol et al., 2014). We use a manual amalgam

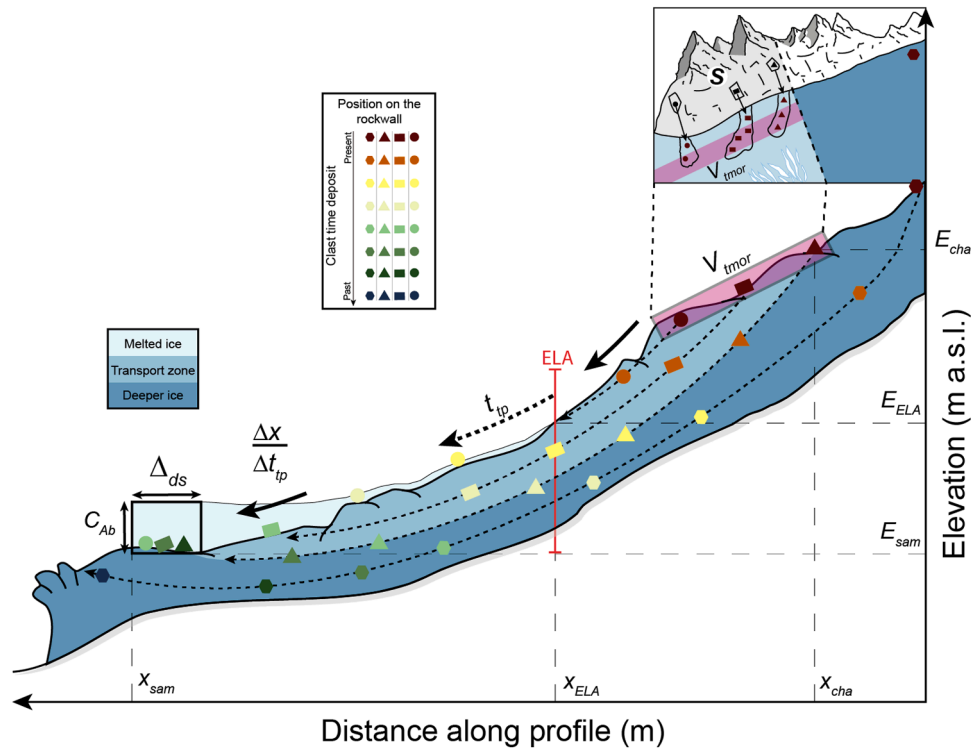


Fig. 4. The various processes and parameters controlling the ^{10}Be concentration of supraglacial clasts (parameters: see Table 1).

protocol where each sample (sand to pebble size, ~1–30 mm) is taken by filling a spoon and where the number of samples is large (hundreds evenly distributed over the sampled area), resulting in a final sample weighing several kilograms.

The map extension of the deposits on the glacier is estimated by superimposing fall-out zones derived from statistical rockfall propagation models (Cathala et al., 2024) with the extent of the glacier (Fig. 1B).

3.2.4. Clasts transported and aggregated by glacier dynamics

The deposits are then embedded in the accumulation zone and flow englacially before emerging in the ablation zone as supraglacial clasts (Dunning et al., 2015) (Fig. 2C). The cumulated ice ablation (C_{Ab} , see Supplementary Material S5.2) progressively aggregated clasts, and the exposure times of clasts located at a point on the surface of a glacier range from zero (for those just released by ablation) to the ice transport time (T_t) from the ELA (for those previously released from the ice at the ELA) (Fig. 4).

Numerous studies have focused on glacier dynamics, and some numerical models couple clast transport with ice flow modeling (Scherler and Egholm, 2020). However, most assume a steady-state dynamic. A decrease in velocity, such as that observed at MdG (Lliboutry and Reynaud, 1981), may invalidate the results obtained from such models. We, therefore, relied on geomorphological markers and mass balance to approximate the MdG dynamics.

We mapped the supraglacial moraines from satellite images (Fig. 1B) to define the flow lines. In addition, as secondary topographic ridges often outline these moraines (Kirkbride and Deline, 2013), we specified their position by calculating the maximum values of the convergence index along the slope gradient using the QGIS software function (Fig. 1D).

Mass balance is expressed by the evolution of ice discharge from the upper to the lower part of the glacier (Bens and Evans, 2010). In this paper, ice flow is calculated from the relationship between elevation and glacier area distribution obtained from the DEM and the relationship between elevation and ablation/accumulation obtained from field measurements (Supplementary Material S5.2). Accumulation rates (A_c),

and ablation rates (A_b) (Fig. 1E) of the MdG have been observed since the end of the 19th century (Glacioclim, 2023; Vincent, 2002; Six and Vincent., 2014). Downstream, the transport time is estimated by counting the annual succession of Forbes bands, a method that considers the significant velocity changes during the 20th century (Lliboutry and Reynaud, 1981). Upstream, the velocities are assumed constant over time as the thickness changes that partly control velocity changes are reduced (Berthier et al., 2014). This assumption enables transport times between two points at the glacier surface (T_t) to be estimated by integrating recent velocity fields (Rabatel et al., 2023; Fig. 1C).

Two types of ice discharges are found, one linked to a mass balance close to an equilibrium state (1954–1981 period; Vincent, 2002) and another one (2018–2022 period, data from Glacioclim) linked to a negative mass balance due to global warming (Vincent et al., 2017).

The 3D flow pattern of the MdG is highly complex, particularly through the large serac zones of the glacier du Géant. It is, therefore, impossible to precisely follow the flow lines and associated transported moraines from the top to the bottom of the glacier. We have limited the estimation of ice-transported clast fluxes to a bulk 2D approach, and we consider the axial line flowing from the summit of Cirque Maudit to be representative of the whole catchment (Fig. 1D, Fig. 5A).

For a portion of a steady-state glacier, a balance of the entering and leaving ice mass is obtained, as illustrated by Eq. (8):

$$\sum_{k=E_{ela}}^{E_{sam}} F_{Ac}(k) \cdot F_{su}(k) = \sum_{k=E_{cha}}^{E_{ela}} F_{Ac}(k) \cdot F_{su}(k) \quad (8)$$

where ablation up to the elevation of a sample (E_{sam}) and accumulation up to an upper elevation (E_{cha}) are equalized on either side of the ELA elevation (E_{ela}). $F_{su}(k)$ and $F_{Ac}(k)$ are respectively the relationships between elevation (k) and glacier area distribution, and the relationship between elevation and ablation/accumulation (Fig. 4).

As with the glacier's mass balance, the flux of rocks leaving the glacier and aggregated by ablation at the surface between E_{sam} and E_{ela} equals the flux of rockfalls entering the deposition surfaces between E_{cha} and E_{ela} . The rockwalls contributing to the fallout deposition zone

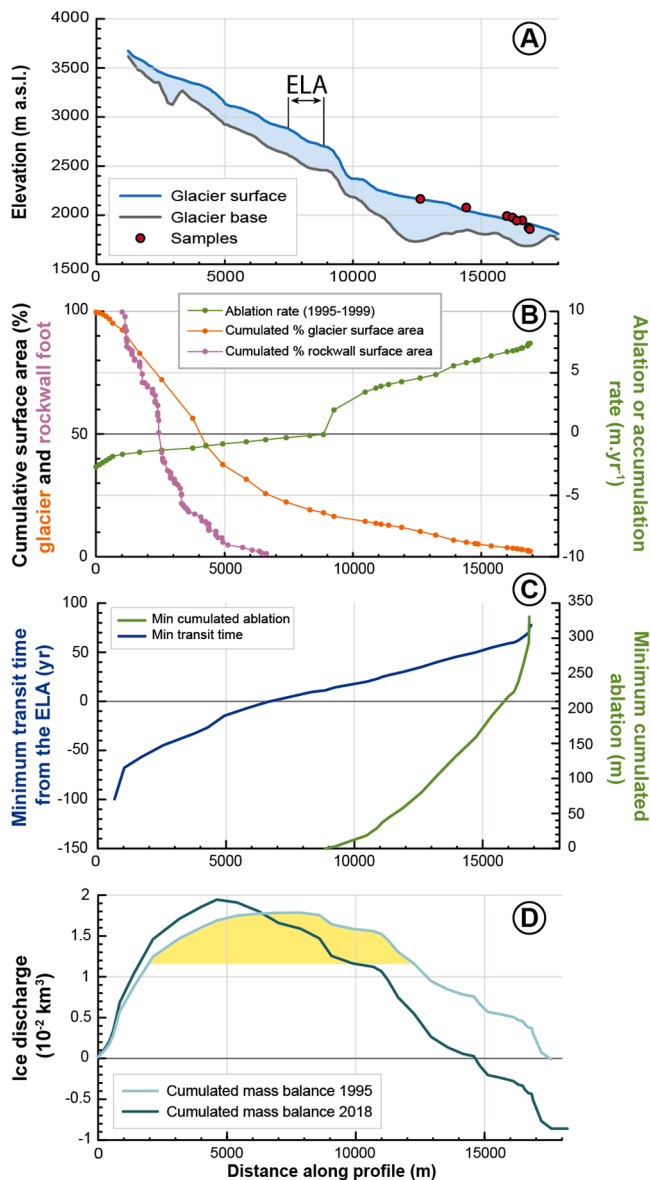


Fig. 5. Glaciological characteristics of the Mer de Glace. (A) Cross-section from the top of the Cirque Maudit to the glacier's tongue (surface topography from IGN DEM; glacier base from Millan et al., 2022). Horizontal arrow: fluctuation of the ELA between 1995 and 2022 (B) Ablation/accumulation (interpolated 1995–1999 glaciological field measurement, from *Glacioclim*); cumulated percentage of the surface area of the glacier (base from IGN DEM) and cumulated percentage of the rockwalls area (S/St) as a function of the distance from the top of the Cirque Maudit. (C) Cumulated ablation and transport time from ELA (calculated from Supplementary Material S5). (D) Ice discharge. Steady cumulated mass balance (-1995 mass balance) and negative mass balance (2018 mass balance). Yellow area: partial mass balance linked to MG18.3 sample (see text).

between E_{ela} and E_{cha} are estimated from mapped rockfall release areas, derived from statistical models (Fig. 4B; Cathala et al., 2024). Assuming a spatially constant erosion rate, the flux of rockfall is considered proportional to the rockwall surface area (S) above the domination the deposition zone. The rockwall flux is normalized by the whole UMdG flux and expressed as (S/S_t) , where (S_t) is the surface area of all contributing rockwalls (Fig. 7B). The dates of the older and younger aggregated rockfalls are estimated from the glacial transport times between E_{cha} and E_{sam} and between E_{cha} and the elevation of lower deposits above the ELA, respectively.

Nonetheless, correction factors must be introduced in the 2D glacier description (see Supplementary Material S5.2), and only the orders of magnitude should be retained for the glacier kinematics. In peculiar, the transverse distribution of the clasts in a glacier has been estimated by assuming that clasts are only concentrated in supraglacial moraines and that the clast composition of a single moraine is homogenous due to the transversal dispersal processes (Kirkbride and Deline, 2013).

The volume of amalgamed rockfall debris in a portion of a moraine is therefore estimated by integrating the flux during the period required to cross this zone and normalized according to the present-day annual production of the whole rockwalls of the UMdG to facilitate the comparison with the present-day period. This leads to the equation:

$$V_{t_{mor}} / Pt = \Delta_{ds} \frac{\Delta T_t}{\Delta x} \frac{S}{St} \frac{L}{Lt} \quad (9)$$

where L is the width of this moraine, Lt is the width of all moraines cumulated in a glacier cross-section, Pt is the present-day annual production of the whole rockwalls, $V_{t_{mor}}$ is the volume of accumulated rockfall debris for a zone where the velocity is $\Delta x/\Delta T_t$, and with high and low boundaries separated by a distance Δ_{ds} . It should be noted that the actual flux of aggregated clasts is greater than that calculated, assuming steady-state conditions, as present-day glaciers have a negative mass balance.

3.2.5. ¹⁰Be concentration and glacial transport

Clasts are shielded from cosmic rays by the ice when its thickness exceeds 10 m (Guillon et al., 2015) but are exposed during supraglacial transport beneath the ELA (Wetterauer and Scherler, 2023). The concentration acquired is therefore approximated by a function of the average nuclide production rate on the glacier, and Eq. (7) becomes:

$$C_0 = \frac{P_{mr} \Delta L_n}{\epsilon_{ml}} + \left(\frac{T_t}{3} + T_p \right) \cdot P_{mr} \quad (10)$$

where P_{mr} is the average nuclide production rate on the glacier, T_t is the ice transport duration from ELA and T_p the exposure period near the glacier surface (Supplementary Material S4.1).

4. Results

4.1. Rockfall inventories

4.1.1. Inventory from the network of observers

The rockwalls representing the source zones of the supraglacial load cover a projected surface area of 3.5 km² (Fig. 1E). 71 rockfalls were identified from satellite images for 2003 (Ravanel et al., 2017) and from the network of observers for 2007–2011 (Ravanel et al., 2010; Supplementary Material S2) (Fig. 6). The associated erosion rate ϵ_{ob} is 3.0 ± 0.6 mm.yr⁻¹, and the most considerable rockfall is 20,000 m³.

The CDM distribution is fitted by a SRFF function with $\bar{a} = (1.8 \pm 0.3) \times 10^{-4}$ rockfall.yr⁻¹.m⁻², $b = 0.83 \pm 0.1$ and $r^2 = 0.7$. For this inventory, V_{Cmi} was chosen to be higher than 200 m³ to exclude the 100 m³ – V_{min} value frequently indicated by observers for small rockfalls of actual volume <100 m³ – and V_{Cma} (24,433 m³) is greater than V_{max} . The erosion rate ϵ_{pl} is then 5.6 ± 1.4 mm.yr⁻¹, with an extrapolated part (ϵ_{sma}) of 2.2 ± 0.6 mm.yr⁻¹ for volumes ≤ 100 m³ of 3.4 ± 0.9 mm.yr⁻¹ for volumes between 100 and 20,000 m³.

4.1.2. Terrestrial laser scanning inventory

Five rockwalls (Fig. 1E) covering a surface area of 0.19 km² have been scanned (Ravanel et al., 2011) in the UMdG (Supplementary Material S1). Their altitudinal distribution ranges from 3320 m to 3842 m a.s.l., averaging 3570 m. Between 2006 and 2011, repeated TLS surveys revealed 123 rockfalls ≥ 1 m³ while the largest has a volume of 566 m³ (Fig. 6). The related erosion rate ϵ_{ob} is 4.0 ± 0.4 mm.yr⁻¹.

The SRFF function, which fits the CDM curve with $r^2 = 0.71$, is

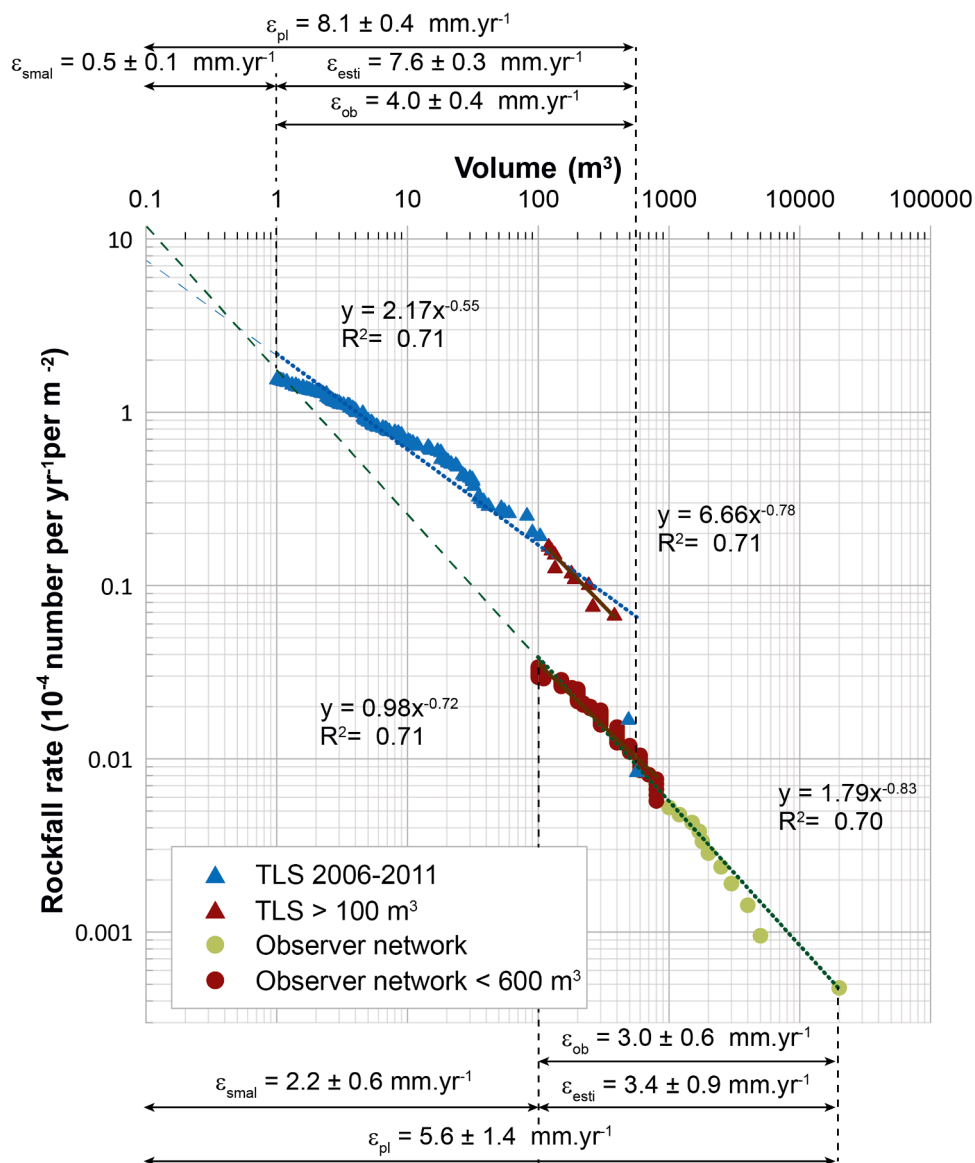


Fig. 6. Comparison of the cumulative volume frequencies of rockfall events estimated by TLS comparison and direct observations for the UMDG.

characterized by a b -value of 0.55 ± 0.05 and a cumulated frequency (\bar{a}) of $2.2 \pm 0.07 \times 10^{-4}$ rockfall.yr $^{-1}$.m $^{-2}$. For this inventory, V_{min} is a completeness value considering the technical choice, and V_{Cmi} has been chosen equal to V_{min} as the coefficient of determination r^2 does not decrease when V_{Cmi} is greater than V_{min} and V_{Cma} ($16,129 \text{ m}^3$) is greater than V_{max} . The erosion rate ϵ_{pl} is then $8.1 \pm 0.4 \text{ mm.yr}^{-1}$, with an extrapolated part (ϵ_{smal}) of $0.5 \pm 0.1 \text{ mm.yr}^{-1}$ for volumes $< 1 \text{ m}^3$, and an estimated part (ϵ_{esti}) of $7.6 \pm 0.3 \text{ mm.yr}^{-1}$ for volumes between 1 and 566 m^3 (Fig. 6).

4.2. Comparison of the two rockfalls inventories

Six rockfalls have been recorded twice in the 100 to 566 m^3 range covered by the two methods when the temporal and spatial coverage were common, confirming the methods' robustness. However, the observations underestimated the TLS-derived volume by an average of 20 %, varying between 3 and 29 %.

Over the common range of volumes, the productivity of rockwalls surveyed by TLS is much higher than that of rockwalls observed by the network: the \bar{a} -values are 6.66 ± 0.5 and 0.98 ± 0.2 , respectively, whereas the estimated b -values are close: 0.78 ± 0.24 and 0.72 ± 0.15 , respectively (Fig. 6).

4.3. Erosion rate inferred from supraglacial nuclide concentration

4.3.1. Sample location and origin of amalgamated clasts

Samples of supraglacial clasts were taken from the downstream part of the MdG to be distributed transversely and longitudinally (Fig. 7A) out of the deposits from rockfalls coming from the side rockwalls (Cathala et al., 2024) or from lateral moraine erosion (Le Roy et al., 2015). The samples are located on Forbes bands b15 to b56 (Fig. 7A). They were taken from the supraglacial moraines over the width of 50 m and longitudinal distances between 154 and 643 m (Table 2).

The UMDG that collects clasts was laterally delimited by tracing from downstream supraglacial moraines (Fig. 7A), two transport lines deduced from topography analysis (dashed line, Fig. 1D). Considering the uncertainty surrounding the transport lines and the extension of the rockfall deposit zones, a distinction was made between "certainly" (red polygons) and "potentially" (black polygons) contributing rockwalls (Fig. 1D). The altitude of the contributing rockwalls ranges from 2960 to 4177 m a.s.l., with an average of 3608 m. The ^{10}Be production rates of the rockwalls range from $35.6 \text{ at.g}^{-1}\text{.yr}^{-1}$ and $78.3 \text{ at.g}^{-1}\text{.yr}^{-1}$ with a mean of $53.1 \text{ at.g}^{-1}\text{.yr}^{-1}$. (Supplementary Material S4.2).

For the uppermost sample (MG18-3- Fig. 7), an ablation of 90–96 m

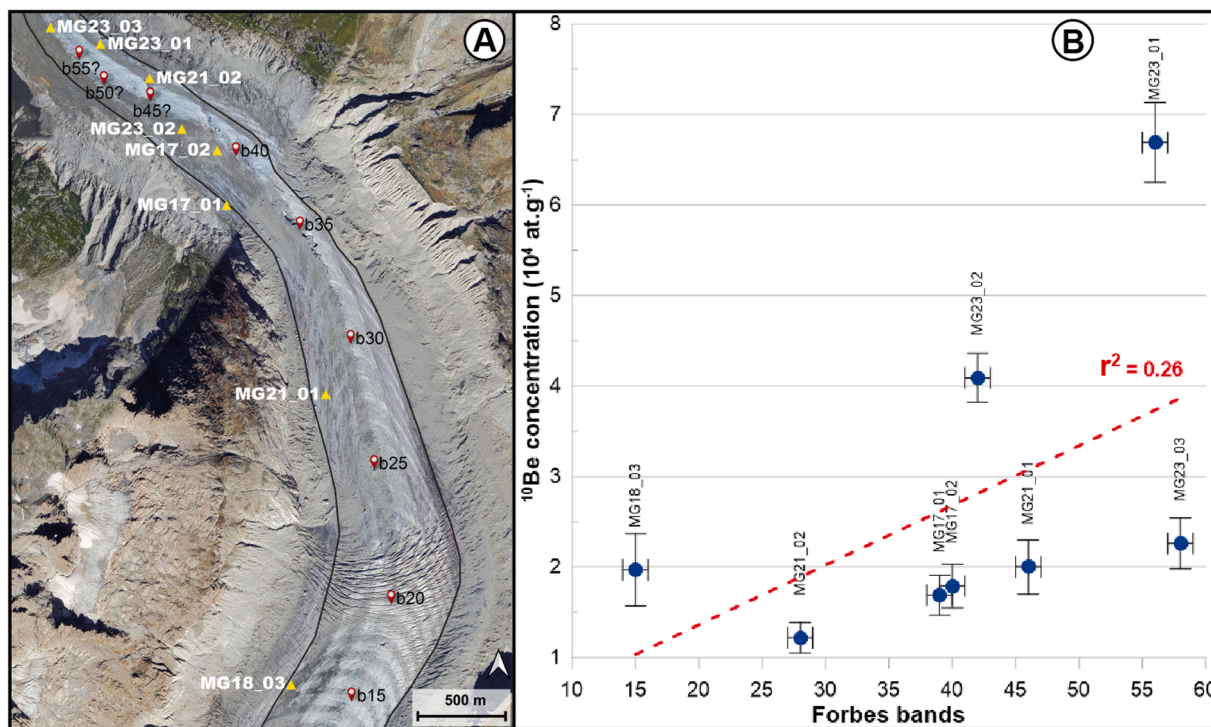


Fig. 7. Measured ^{10}Be concentration by sample position on the Mer de Glace. (A) ^{10}Be samples and Forbes bands (satellite image September 2015). Forbes band numbers b1 to b55 refer to the counting of alternating white and grey bands with a year periodicity (b1 refers to the yellow dot on Fig. 1C). (B) x-axis: Forbes band number on Fig. 7a. The 1σ analytical uncertainty is shown for each value. Red dashed line: linear fit with all samples.

accumulates clasts whose exposure times at the glacier surface vary from zero (for those just released by the ablation) to 42 years (for those released from the ice at the ELA) (Table 2). For the lowermost sample (MG23–3 – Fig. 7), 185–366 m ablation accumulates clasts with exposure times at the glacier surface between 0 and 85 years. Partial mass balance (yellow zone, Fig. 5D) shows that MG18–3 corresponds to rockfalls deposited below 3400 m a.s.l. in the period 1913–1987, while MG23–3 corresponds to rockfalls deposited below 3700 m a.s.l. in the period 1820–1949. Finally, each sample accumulates clast flux that amalgamates rockfalls from 9 to 22 % of the whole annual UMdG rockfall production (Table 2).

4.3.2. ^{10}Be concentration of samples

The concentration acquired during supraglacial transport was estimated as a function of the transport time under the ELA (Fig. 5C) and an average production rate of $24 \text{ at.g}^{-1} \cdot \text{yr}^{-1}$ at 2200 m a.s.l. It ranges between 0.06 and $0.12 \times 10^4 \text{ at.g}^{-1}$, a value less than half the analytical uncertainty on concentrations (0.17 to $0.44 \times 10^4 \text{ at.g}^{-1}$) (Table 2).

Measurements of ^{10}Be concentrations range from 1.22×10^4 to $6.69 \times 10^4 \text{ at.g}^{-1}$. Their arithmetic mean is $2.7 \pm 0.3 \times 10^4 \text{ at.g}^{-1}$, and their average weighted by the number of rockfalls probably amalgamated in each sample (Table 2) is $3.6 \pm 0.4 \times 10^4 \text{ at.g}^{-1}$. There is no trend associated with the transverse position: the three strong values above the regression line are located on the left, the center, and the right parts of the glacier, respectively. A downstream increase in ^{10}Be concentrations could be suggested in Fig. 7, but the best fit is characterized by a small r^2 of 0.26 (Fig. 7B). Without the two outliers, there would be no trend in concentration downstream of the glacier and the mean concentration would be lower; nevertheless, such a selection is rather subjective as it is based solely on visual consideration and leads to the elimination of samples that have statistically amalgamated the greatest number of rockfalls (Table 2). Therefore, the arithmetic mean and average weighted concentrations are used to estimate the erosion rates in the discussion section (Table 3).

5. Discussion

5.1. Estimation of sub-actual erosion based on the two types of rockfall inventory

Poisson's law predicts that an under-occurrence of rare and important events may occur over a short observation period. This under-occurrence slightly influences the b -value estimate but strongly influences the total volume estimate due to the large volume of rare events. The observed rate (ϵ_{ob} of $4.0 \pm 0.4 \text{ mm.yr}^{-1}$) and the estimated rate (ϵ_{esti} of $7.6 \pm 0.3 \text{ mm.yr}^{-1}$) from TLS records differ significantly, likely due to an under-representation of observed events within the 350 and 566 m^3 vol range, which was subsequently corrected for data collected during 2011–2015. This suggests that numerous biases affect inventories acquired during short observation periods, and power law integration is a powerful method in erosion rate estimation.

Threshold values used in the employed methods hinder the small volumes, leading to underestimating the erosion rate (Grabert and Santi, 2022). This underestimation can be approached using the SRFFF function. For the inventory carried out by the network of observers, estimates of ϵ_{small} and ϵ_{esti} suggest that the erosion rate is underestimated by 64 % because rockfalls $< 200 \text{ m}^3$ are excluded. Conversely, ϵ_{esti} underestimates the erosion rate by 6.5 % for the TLS, where rockfalls of $< 1 \text{ m}^3$ are excluded.

Nonetheless, extrapolation on a very large domain of a SRFF is misleading. The direct extrapolation of the power laws on the whole domain between 1 and 20,000 m^3 gives a probably unrealistic erosion rate ϵ_{pl} of $40.0 \pm 3.0 \text{ mm.yr}^{-1}$ for the TLS. A robust estimate of the total erosion rate, therefore, requires an analysis of the differences and complementarities between the two catalogs.

Both inventories are reliable and statistically representative in the two distinct intervals from 1 to 566 m^3 and from 200 to 20,000 m^3 , with different b -values, respectively 0.55 ± 0.1 and 0.83 ± 0.1 (Fig. 6). Nevertheless, the b -values calculated for the overlapping interval of the two inventories are not significantly different, with a value close to 0.75.

Table 1
Parameters and acronyms used in the paper.

Symbol	Description	Unit
CDM	Cumulative Distribution Magnitude of the rockfall volume	Succession of data
SRFF	Specific Rockfall Frequency Function	Continuous function
S	Rock wall area (projected horizontally)	m^2
St	Surface area of the whole rockwalls	m^2
V	Rockfall volume	m^3
T	Period of observation or exposition	yr
$f_{mor}(V)$	Cumulative distribution of rockfalls aggregated in a moraine	–
$fs(V)$	Cumulative frequency of rockfalls for an area (power law)	$yr^{-1} \cdot m^{-2}$
V_{mp}	Potential greatest volume of rockfalls	m^3
V_{max}	Maximum observed volume of rockfalls	m^3
V_{min}	Minimum observed volume of rockfalls	m^3
V_{Cmi}	Minimum cutoff volume used in the power law fit	m^3
V_{Cma}	Maximum cutoff volume used in the power law fit	m^3
N_O	Number of rockfalls with a volume $> V_{Cub}$	–
V_{tob}	Sum of the volumes of observed rockfalls	m^3
V_{tp}	Total volume inferred from integrating the power law	m^3
Pt	Annual production of the whole rockwalls of the BG	$m^3 \cdot yr^{-1}$
V_{tmor}	Volume of the rockfalls aggregated in a moraine	m^3
D_{max}	Maximum thickness of the rockfalls	m
A	Number of rockfalls $> 1 m^3$ (power law)	–
\bar{A}	Frequency of rockfalls $> 1 m^3$ per surface unit (power law)	$yr^{-1} \cdot m^{-2}$
B	Power law exponent	–
r^2	Coefficient of determination	–
SSe	Residual sum of squares	–
SSr	Regression sum of squares	–
ϵ	Erosion rate	$mm \cdot yr^{-1}$
Rr	Retreat rate (perpendicular to the face)	$mm \cdot yr^{-1}$
ϵ_{ob}	Erosion rate deduced from rockfall inventories	$mm \cdot yr^{-1}$
ϵ_{pl}	Erosion rate estimated from the power law	$mm \cdot yr^{-1}$
ϵ_{infer}	Erosion rate extrapolated from the power law between V_{Cma} and V_{mp}	m^3
ϵ_{esti}	Erosion rate from a fit of the power law between two volume values	m^3
ϵ_{smal}	Erosion rate extrapolated from the power law between 0 and V_{Cmi}	m^3
S_g	Surface area of the glacier	km^2
Ac or Ab	Accumulation rate (positive value) or ablation rate (negative value)	m/yr
C_{Ab}	Cumulated ablation	m
$FAc(E)$	Relationship between elevation and ablation	–
$Fsu(E)$	Relationship between elevation and glacier surface area distribution	–
E_{cha}	Upper elevation of part of glacier subject to local glacier mass balance	m a.s.l.
E_{ela}	ELA elevation	m a.s.l.
E_{sam}	Sample elevation	m a.s.l.
Δ_{ds}	Distance between the two ends of the sampled zone	m
L	Width of the sampled moraine	m
Lt	Width of all the moraines cumulated in a glacier cross-section	m
ϵ_{ml}	Steady-state erosion rate (nuclide approach)	$mm \cdot yr^{-1}$
Z	Depth below the surface	m
$C(z)$	^{10}Be concentration as a function of depth	$atoms \cdot g^{-1}$
P_O	^{10}Be surface production rate	$atoms \cdot g^{-1} \cdot yr^{-1}$
ρ	Density	$Kg \cdot m^{-3}$
P_{mr}	Mean production rate of a rockwall	$atoms \cdot g^{-1} \cdot yr^{-1}$
C_O	^{10}Be measured concentration	$atoms \cdot g^{-1}$
λ	Absorption mean free path	$g \cdot m^{-2}$
λ_{1n}	Mean attenuation length (n for neutrons)	–
P_{mt}	Mean production rate during transport	$atoms \cdot g^{-1} \cdot yr^{-1}$
T_t	Mean transport time of the clasts at the glacier surface	yr
T_p	Exposure time of the clasts close to the glacier surface	yr

This common value would correspond to a continuous function, common to both inventories, with an evolution of the b -value from 0.83 for rockfalls greater than $566 m^3$ to 0.55 for rockfalls $< 566 m^3$. As the b -

value partly reflects the fractal distribution of initial boulder fragmentation (Turcotte, 1986), such variability of b -values across the whole range could suggest a scale-dependent change in the processes and geometry leading to rock mass failure (Malamud and Turcotte, 2006), although our results are too tenuous to confirm such an interpretation definitively.

However, the productivity of the TLS rockwalls (\bar{a}) is 5.1 times greater on the overlapping interval. This greater productivity is considered a local result as the TLS surveyed rockwalls ($0.19 km^2$) constitute only 5 % of the rockwalls of the observer network ($3.5 km^2$), and their productivity is diluted within the lower production of the observer network zone. This great productivity of the TLS rockwalls could be linked to their specific elevation range (3320 to 3842 m a.s.l.) where the permafrost degradation is particularly intense (Magnin et al., 2017) and, at least for some of the rockwalls, to the diminution of their permanent snow cover (Courtial-Manent et al., 2024).

We therefore consider that the TLS study gives a valuable estimate of the b -value for the cumulative distribution of the small (less than $100 m^3$) blocks in the MBM but that the \bar{a} -value cannot be extrapolated at a larger scale. At the scale of the whole MdG catchment, the CDM issued from the observer network is only formed of blocks greater than $100 m^3$, and we extrapolate it towards smaller volumes by using the b value evolution from the TLS rockwalls. As a change in the productivity factor preserves the form of a CDM distribution and only induces a translation of its representation in a classic log-log graphic, a continuous but composite CDM distribution (Fig. 8A) has been represented by weighting by a 1/5.1 factor the volume issued from the TLS inventory, to test various SRFF.

This composite CDM appears as a generally concave curve in a logarithmic diagram (Fig. 8A). Nevertheless, a single SRFF derived from this composite CDM and expressed as “ $y = 0.5 \times x^{-0.61}$ ” provides r^2 and σ_b values (0.71 and 0.04 respectively) that suggest that a single power law, spanning more than four orders of magnitude, is still a reasonable approximation to the distribution of rockfall volumes. Integration of this SRFF yields an erosion rate of $6.1 \pm 2 mm \cdot yr^{-1}$.

SRFFs that approximate the weighted CDM and are formed from two successive power laws minimize the erosion estimate. In particular, the two-segment power law, with the empirical cut-off value of $100 m^3$ between the b -values of 0.42 and 0.91, provides a minimum erosion ϵ_{pl} of $4.1 \pm 1.5 mm \cdot yr^{-1}$ in the volume range below $20,000 m^3$.

5.2. Estimating rockwall erosion rates from cosmogenic nuclide concentration

Wetterauer and Scherler (2023) have shown that the ^{10}Be concentrations acquired during supraglacial transport could be in the same order of magnitude as those obtained from the rockwalls. At MdG, estimates of concentrations acquired during transport are lower than the analytical uncertainty (Table 2), and measured concentrations are considered acquired in the rockwall. Fluctuations in measured concentrations between 1.22 and $6.69 \times 10^4 at \cdot g^{-1}$ may be from local incorporation of high-concentration parts of the rockwall that had failed after a long return time between events. Alternatively, they could be related to variations in erosion rates. The downstream increase in concentrations, weakly suggested by our data, could align with an increase in erosion intensity over time. However, the number of rockfalls amalgamated in each sample corresponds to < 2.2 years of rockfall production at UMdG, suggesting that these fluctuations reflect the records of a short rockfall production period. Therefore, only an average erosion rate of all the UMdG rockwalls is estimated from all the ^{10}Be concentrations (Orr et al., 2021). Approximately 800 rockfalls are $> 1 m^3$, (from the sum of the columns in Table 2) equivalent to 7 years of UMdG rockfall production are then amalgamated in all the samples and erosion rates of $1.25 mm \cdot yr^{-1}$ and $0.94 mm \cdot yr^{-1}$ are found from the arithmetic mean or the weighted average concentrations (Eq. (10)). The uncertainty surrounding these erosion rates has been estimated by adding together the relative uncertainties associated with:

Table 2

Supraglacial sample characteristics. Due to the 2D description of glacier dynamics, only the orders of magnitude should be retained for the dates, E_{cha} , S/S_t , L/L_0 , and $V_{t_{mor}}/Pt$. For $V_{t_{mor}}/Pt$, only the maximum estimate is indicated. Details of the ^{10}Be sample location and chemistry are available in Supplementary Material S4.

		Geomorphology		Glacier dynamics		Clasts transport		^{10}Be Measurement			
Forbes bands	L/L_t Width sampled moraine/ cumulative width of all moraines	Δ_{ds} Length of the sampled zone	t_{tp} Ice transport time from the ELA	C_{ab} Cumulated ablation	Period of rockfall	E_{cha} Max elevation of the collected deposits	$V_{t_{mor}}/Pt$ Equivalent annual UMDG rockfall production amalgamated in samples	$\bar{A}.S.V_{t_{mor}}/Pt$ Amalgamated rockfalls (> 1m ³)	$t_{tp}.P_{mt}$ ^{10}Be produced during transport	C_0 ^{10}Be and 1 σ analytical uncertainty	
Sample	Number	%	m	yr	m	yr	m a.s.l.	yr	Number	10 ⁴ at.g ⁻¹	10 ⁴ at.g ⁻¹
MG17_01	39	10	170	66 ± 7	161–233	1865–1962	3550	0.1	11	0.09	1.7 ± 0.2
MG17_02	40	30	255	67 ± 7	163–240	1864–1961	3580	0.4	50	0.09	1.8 ± 0.2
MG18_03	15	20	195	42 ± 7	90–96	1913–1987	3330	0.2	21	0.06	2.0 ± 0.4
MG21_01	46	14	154	73 ± 7	170–281	1873–1959	3590	0.4	49	0.10	2.0 ± 0.3
MG21_02	28	17	326	55 ± 7	150–163	1891–1977	3560	0.3	37	0.08	1.2 ± 0.2
MG23_01	56	12	515	83 ± 7	173–353	1822–1951	3595	1.3	165	0.11	6.7 ± 0.4
MG23_02	42	25	653	69 ± 7	164–253	1836–1965	3610	2.2	277	0.10	4.1 ± 0.3
MG23_03	58	17	440	85 ± 7	185–366	1820–1949	3617	1.6	203	0.12	2.3 ± 0.3

Table 3

Summary of erosion rates obtained by the different methods (cosmogenic ^{10}Be for long-term, observer network and TLS catalog for short-term) and different periods in the UMDG catchment.

Long-term summary		
	Surface area (horizontal projection)	3.5 km ²
	Arithmetic mean ^{10}Be concentration of the supraglacial clasts	$2.7 \pm 0.3 \cdot 10^4$ at.g ⁻¹
	Mean ^{10}Be production in the rockwalls	53.1 at.g ⁻¹ yr ⁻¹
	Mean ^{10}Be production during transport beneath the ELA	20 at.g ⁻¹ yr ⁻¹
	Mean transport time below the ELA	60–74 yr
	Mean transport time above the ELA	22–36 yr
	Estimation of the period when the sampled rockfalls occurred	Between 1822 and 1987
	Period on which the erosion rate is averaged before the rockfall ^{10}Be long-term erosion	400–560 yr 0.2 – 2.2 mm.yr⁻¹
Short-term summary	Observers catalog	TLS
Period	2003 and 2007 to 2011	2006–2011
Surface area (horizontal projection)	3.5 km ²	0.19 km ²
Cumulated rockfall volume	63,030 m ³	4229 m ³
Volume of the greatest event	20,000 m ³	566 m ³
Volume of the smallest observed event	100 m ³	0.2 m ³
Volume of the smallest considered event	200 m ³	1 m ³
Number of events	71	123
a : productivity (number of events greater than 1 m ³)	$1.7 \cdot 10^{-4}$ m ² yr ⁻¹	$2.1 \cdot 10^{-4}$ m ² yr ⁻¹
b : (exponent power law)	0.82 ± 0.1	0.55 ± 0.1
ϵ_{ob} : erosion inferred from cumulated volume	3.0 ± 0.6 mm.yr⁻¹	4.0 ± 0.4 mm.yr⁻¹

(#1) the 1 σ uncertainty on the analytical measurement (-13 %; from Supplementary Material S4.2); (#2) the uncertainty on the production rate calculation (-10 % considering that the absence of shielding compensate the effect of snow cover, see Supplementary Material S4.2), (#3) the uncertainty on the origin of the rockfalls (47 %, assuming unrealistically that all rockfalls originate from either the upper or lower part of the rock face, see Supplementary Material S4.2), and (#4) the error due to the application of Eq. (7) to a series of stochastic rockfall events (-10 % from Ward and Anderson, 2011). Under these conditions, the total relative error on the ^{10}Be erosion rate reaches 80 %, and we conservatively consider that the most probable ^{10}Be erosion rates of 1.25 mm.yr⁻¹ and 0.94 mm.yr⁻¹ to be between 2.2 and 0.2 mm⁻¹.

A sample amalgamates a limited number of rockfalls (Table 2) as the collection window shifts in space over time. As a result, the rockfalls in each sample extend temporally throughout the order of a century (Table 2), covering in total, from the summation of all the samples, the period 1820–1987. Furthermore, the production of ^{10}Be in the rockwalls precedes the rockfall events and occurs over the nuclide integration time ($\lambda_{10}\text{Be}/\epsilon_{ml}$) necessary to erode the attenuation length (von Blanckenburg,

2006). Given the average ^{10}Be erosion rate, the period required to erode 60 cm thickness is 500 years, and taking into account uncertainties in this erosion rate, it is between 300 and 3000 years. The ^{10}Be erosion rate, therefore, takes into account erosion over a multi-centennial span, which predates the present by several decades to two centuries. The average erosion rate calculated using ^{10}Be , thus, corresponds to a period covering the entire Little Ice Age (LIA), which lasted between the 15th and 19th centuries (Robock, 1979).

5.3. Recent increase in erosion rates

A >200 % increase in erosion rate is estimated between the LIA and the period 2003–2011 (from 1.2 to 4.1 mm.yr⁻¹), and even a very conservative estimate of the errors still proves a >150 % increase (from ≤ 1.4 mm.yr⁻¹ to ≥ 2.2 mm.yr⁻¹). Such an increase does not contradict the hypothesis of a ^{10}Be steady-state erosion during LIA, given the time lag between the periods covered by the inventories and the ^{10}Be radioactive decay. This increase could be linked to a temperature-related destabilization following climate change (Gruber

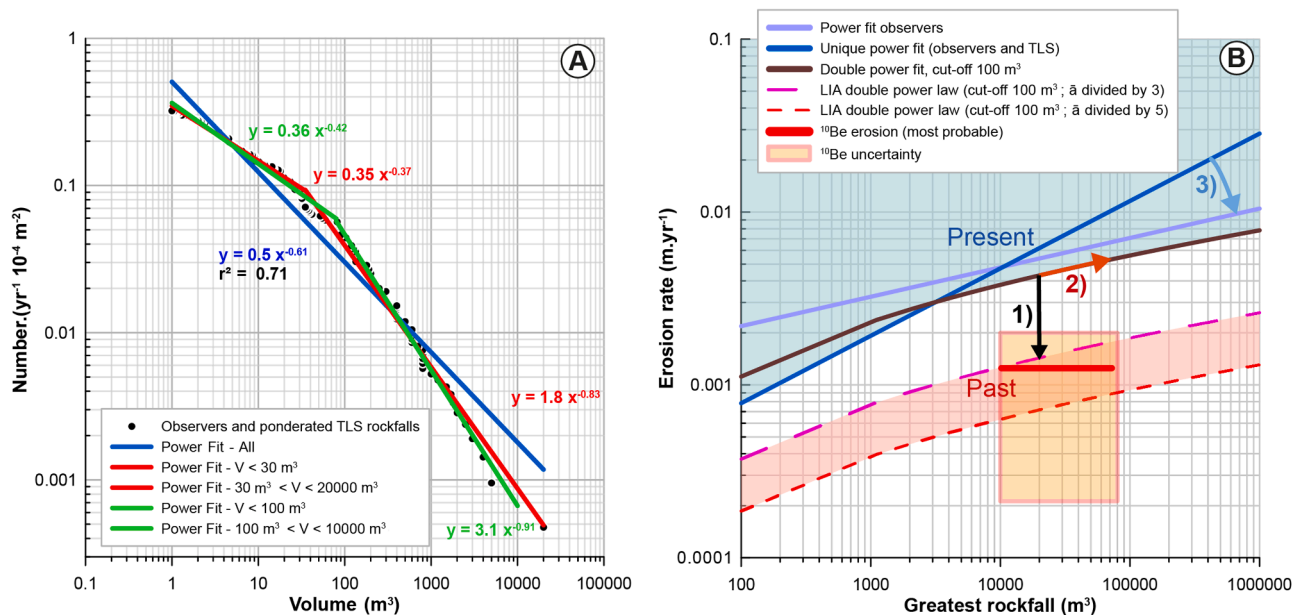


Fig. 8. (A) A composite cumulative rockfall frequency for the UMDG rockwalls. The volumes obtained by TLS were weighted by $1/5.1$ to form a rockfall distribution (black dots) in continuity with that of the observers. A unique SRFF is issued from this weighted CDM (blue power fit). Two-part power laws are also shown (with cut-offs at 30 and 100 m^3 , respectively) to estimate a minimum erosion rate. (B) Relationships between the maximum volume of the rockfalls, erosion rate, and rockfall distribution power law parameters, calculated using Eq. (4). Blue zone for present solutions domain, pink for past solution domain. Black arrow (1): influence of a decrease of the \bar{a} -value; red arrow (2): influence of an increase of the value of the greatest rockfall (V_{mp}); blue arrow (3): influence of an increase of the b -value. Maximum and minimum ^{10}Be erosion rates, respectively, from arithmetic mean and weighted average concentrations.

and Haerberli, 2007) when permafrost-affected rockwalls become unstable due to changes in the rock-ice-mechanical relationships (Krautblatter et al., 2013).

Such an increase in rockfalls since the LIA has already been envisaged by studies in the MBM (Ravanel and Deline, 2008) or the Caucasus mountains (Haerberli et al., 2004). Our study emphasizes its significance within the setting of the third largest glacier in the Alps, suggesting a ~ 3 -fold increase in the rate of rockfalls (indicated by an increase in the \bar{a} -value). This assumption is made under the condition that the distribution of volumes (i.e., b -value) and the maximum volume (V_{Cma}) are constant and equal to those observed (Fig. 8B, arrow (1)). A past variation in b -value cannot be ruled out (Fig. 8B, arrow (3)). However, the case of Tour Ronde, with an 800 % increase in annual volumes without a clear evolution in the b -value (Courtial-Manent et al., 2024), does not support this hypothesis.

The erosion studies carried out using inventories and ^{10}Be measurements take into account cumulative volumes corresponding to five years and around seven years of UMDG production, respectively. Furthermore, considering a ~ 300 % increase in erosion rates, the number of amalgamated rockfalls in all ^{10}Be samples is equivalent to < 2.3 years of sub-actual production from the UMDG rock faces. Subactual TLS and ^{10}Be erosion rates are, therefore, both estimated over periods of a few years, and both erosion rates may be underestimated due to the absence of larger volumes with a high return time (arrow (2) in Fig. 8B).

5.4. Influence of very large rockfalls

The observation of large volumes is biased due to their recurrence time exceeding the inventory period (Mavrouli and Corominas, 2020). However, the role of large volumes is fundamental in estimating the representative, longer term average erosion rates. Power law extrapolation is reliable up to a V_{Cma} of $77,000$ m^3 in the MBM from a catalog covering the surface of the entire massif (Sarr et al., 2019; Supplementary Material S3). Extrapolating the SRFF from the surveys beyond the observed V_{max} (20×10^3 m^3) at UMDG till a V_{Cma} of $77,000$ m^3 increases the erosion rate ε_{pl} by 30 % and ε_{pl} reaches 5.5 mm.yr^{-1} (Fig. 8B).

V_{Cma} volume of 10^6 m^3 is similar to the largest rockfalls on the southern slopes of MBM (Deline et al., 2015), and that cannot be excluded as *a priori* in our study area. Indeed, the rockwalls of the UMDG are characterized by the same lithology, extent as the southern slopes of the MBM (~ 700 m high), and the largest rockfall volumes notably depend on the rockwall's dimensions and other intrinsic characteristics (Hantz et al., 2003; Brideau et al., 2009). Estimation of ε_{pl} would be almost doubled using the power law extrapolation, but such a volume is out of the proved domain of the power law (Coles, 2004).

However, the ^{10}Be erosion estimate did not provide evidence for very large rockfalls, as the recent increase in the rate of rockfalls masks their potential influence (Fig. 8). Furthermore, our analysis shows that the amalgamated clasts are equivalent to ~ 7 years of UMDG rockfall production, i.e., in the same order of magnitude as the production of the period 2003–2022, when the largest rockfall was $20,000$ m^3 . In other words, ^{10}Be erosion, although considered over an ancient period, does not necessarily represent long-term erosion.

6. Conclusion

We used data from three approaches to assess erosion rates' temporal and spatial evolution. TLS reiteration provides inventories of low-volume rockfalls (typically < 1000 m^3) with good spatial accuracy but is limited to specific areas and timeframes. Direct observations cover larger areas and provide precise event dates, excluding the smallest rockfalls (< 100 m^3). Cosmogenic nuclides only provide an average value of erosion rate over time periods and surfaces, equivalent to < 10 years of rockfall production on all the rockwalls considered. To compare the results of these methods, it was necessary to clarify the significance of the different erosion rate estimates. We used a mathematical integration of the power law describing the cumulative distribution of observed volumes to compare them systematically. By normalizing it by the rockwall surface and observation time, we proposed a method for providing an integrated long-term erosion rate.

Our work shows that block falls < 1 m^3 account for < 6 % of rockfall volumes, whereas rockfalls smaller than 100 m^3 account for a significant

proportion. Since direct observations do not include volumes $< 100 \text{ m}^3$, we have estimated them using results from TLS reiteration, weighted by rockwall specificities, suggesting that rockfalls under 100 m^3 account for $>20 \%$ of the total.

Overall, our estimates for the period 2006–2011 indicate a total erosion rate ranging from 4.1 to 5.6 mm.yr^{-1} . This comprises approximately 1 mm.yr^{-1} linked to rockfalls $< 100 \text{ m}^3$, the rest for rockfalls whose volume is less than the largest observed ($20,000 \text{ m}^3$). However, the local erosion rate of some rock faces is up to 500 % higher than that of all rock faces in the UMDG basin.

In addition, an analysis of the transport conditions of the clasts before their sampling in supraglacial position allows us to assess the representativeness of the measured ^{10}Be concentrations. This analysis is based on a glaciological mass balance model incorporating numerous observations from the MdG. It provides an order of magnitude for the total number of rockfalls amalgamated in the supraglacial load and shows that aggregated rockfalls fell during a long time – but with a rather small total volume – equivalent to a few years of the whole UMDG production. To maximize the number of amalgamated rockfalls, we adopted an approach in which only the average erosion rate of the entire area is estimated. Fluctuations in the ^{10}Be concentrations of the samples collected at different points are considered to reflect the stochastic aspect of the rockfalls. An erosion rate ranging from 0.2 to 2.2 mm.yr^{-1} is found.

Comparison between the minimum erosion rate estimated from inventories and the ^{10}Be erosion rate indicates that the erosion rate in the UMDG has increased 3-fold between the period before the beginning of the 20th century and the beginning of the 21st century (2006–2011). Continuous observations in this area will enable us to estimate the magnitude of this increase more accurately in the future.

CRediT authorship contribution statement

Léa Courtial-Manent: Writing – review & editing, Writing – original draft, Visualization, Software, Resources, Methodology, Formal analysis, Data curation. **Jean-Louis Mugnier:** Writing – review & editing, Writing – original draft, Validation, Supervision, Resources, Project administration, Funding acquisition, Formal analysis, Data curation. **Ludovic Ravanel:** Writing – review & editing, Validation, Supervision, Resources, Formal analysis, Data curation. **Julien Carcaillet:** Writing – review & editing, Methodology. **Philip Deline:** Writing – review & editing, Resources, Conceptualization. **Jean-François Buoncrisiani:** Writing – review & editing, Visualization, Software, Methodology, Funding acquisition.

Declaration of competing interest

The authors declare that they have no known competing financial interests or personal relationships that could have appeared to influence the work reported in this paper.

Acknowledgments

The ASTER team is warmly thanked for cosmogenic nuclide analyses performed at the ASTER AMS facility (CEREGE, Aix-en-Provence) and R. Vassallo for his advice on chemical preparations. Thanks to L. Moreau and A. Lhosmot for accompanying us in the field, to A. Schwing and M. Cathala for their insights, and to all the members of the Glacioclim National Observation Service (SNO) of the Institut National des Sciences de l'Univers (INSU) for sharing glaciological data. We also thank the editor and the two reviewers for their valuable feedback, which helped improve this paper. L. C.-M.'s thesis is funded by grants from Labex OSUG (Grenoble Observatory) and USMB (Université Savoie-Mont-Blanc). This work contributes to the INSU Tellus project (MORCLIM-YDNG; 2024).

Supplementary materials

Supplementary material associated with this article can be found, in the online version, at [doi:10.1016/j.epsl.2024.119142](https://doi.org/10.1016/j.epsl.2024.119142).

Data availability

Data is available in the Supplementary Materials file.

References

- Adler, C., Huggel, C., Orlove, B., Nolin, A., 2019. Climate change in the mountain cryosphere: impacts and responses. *Reg. Environ. Change* 19, 1225–1228. <https://doi.org/10.1007/s10113-019-01507-6>.
- Aki, K., 1965. Maximum likelihood estimate of b in the formula $\log N = a - bM$. *Bull. Earthquake Res. Inst. (University of Tokyo)* 43, 237–239.
- Ballantyne, B.K., 2002. Paraglacial geomorphology. *Quaternary Sci. Rev.* 21, 1935–2017.
- Bens, D., Evans, D., 2010. *Glaciers and glaciation*. Hodder Education edition 788.
- Beniston, M., 2003. Climatic change in mountain regions: a review of possible impacts. *Clim. Chang. Adv. Global Change Res.* 59, 5–31. https://doi.org/10.1007/978-94-015-1252-7_2.
- Berthier, E., Vincent, C., Magnússon, E., Gunnlaugsson, Á.Þ., Pitte, P., Le Meur, E., Masiokas, M., Ruiz, L., Pálsson, F., Belart, J.M.C., Wagnon, P., 2014. Glacier topography and elevation changes derived from Pléiades sub-meter stereo images. *Cryosphere* 8, 2275–2291. <https://doi.org/10.5194/tc-8-2275-2014>.
- Biskaborn, B.K., Smith, S.L., Noetzi, J., Matthes, H., Vieira, G., Streletskiy, D.A., Schoeneich, P., Romanovsky, V.E., Lewkowicz, A.G., Abramov, A., Allard, M., Boike, J., Cable, W.L., Christiansen, H.H., Delaloye, R., Diekmann, B., Drozdov, D., Etzelmüller, B., Grosse, G., Guglielmin, M., Ingeman-Nielsen, T., Isaksen, K., Ishikawa, M., Johannsson, M., Johannsson, H., Joo, A., Kaverin, D., Kholodov, A., Konstantinov, P., Kröger, T., Lambiel, C., Lanckman, J.-P., Luo, D., Malkova, G., Meiklejohn, I., Moskalenko, N., Oliva, M., Phillips, M., Ramos, M., Sannel, A.B.K., Sergeev, D., Seybold, C., Skryabin, P., Vasiliev, A., Wu, Q., Yoshikawa, K., Zheleznyak, M., Lantuit, H., 2019. Permafrost is warming at a global scale. *Nat. Commun.* 10, 264. <https://doi.org/10.1038/s41467-018-08240-4>.
- Braucher, R., Bourlès, D., Merchel, S., Vidal Romani, J., Fernandez-Mosquera, D., Marti, K., Léanni, L., Chauvet, F., Arnold, M., Aumaître, G., Keddadouche, K., 2013. Determination of muon attenuation lengths in depth profiles from *in situ* produced cosmogenic nuclides. *Nucl. Instrum. Methods Phys. Res. Section B* 294, 484–490. <https://doi.org/10.1016/j.nimb.2012.05.023>.
- Brideau, M.-A., Yan, M., Stead, D., 2009. The role of tectonic damage and brittle rock fracture in the development of large rock slope failures. *Geomorphology* 103, 30–49. <https://doi.org/10.1016/j.geomorph.2008.04.010>.
- Bussy, F., Schaltegger, U., Marro, C., 1989. The age of the Mont-Blanc granite (Western Alps): a heterogeneous isotopic system dated by Rb–Sr whole rock determinations on its microgranular enclaves. *Schweiz. Mineral. Petrogr. Mitt.* 69, 3–13.
- Cathala, M., Magnin, F., Ravanel, L., Dorren, L., Zuanon, N., Berger, F., Bourrier, F., Deline, P., 2024. Mapping release and propagation areas of permafrost-related rock slope failures in the French Alps: a new methodological approach at regional scale. *Geomorphology* 448, 109032. <https://doi.org/10.1016/j.geomorph.2023.109032>.
- Chmeleff, J., Von Blanckenburg, F., Kossert, K., Jakob, D., 2010. Determination of the ^{10}Be half-life by multicollector ICP-MS and liquid scintillation counting. *Nucl. Instrum. Methods Phys. Res. Section B* 268, 192–199. <https://doi.org/10.1016/j.nimb.2009.09.012>.
- Coles, S., 2004. *An Introduction to Statistical Modeling of Extreme Values*, Springer Series in Statistics. Springer, London, London. <https://doi.org/10.1007/978-1-4471-3675-0>.
- Cossart, E., Braucher, R., Fort, M., Bourlès, D.L., Carcaillet, J., 2008. Slope instability in relation to glacial debuitressing in alpine areas (Upper Durance catchment, southeastern France): evidence from field data and ^{10}Be cosmic ray exposure ages. *Geomorphology* 95, 3–26. <https://doi.org/10.1016/j.geomorph.2006.12.022>.
- Courtial-Manent, L., Ravanel, L., Mugnier, J.-L., Deline, P., Lhosmot, A., Rabatel, A., Duval, P.-A., Batoux, P., 2024. 18-years of high-Alpine rock wall monitoring using terrestrial laser scanning at the Tour Ronde east face, Mont-Blanc massif. *Environ. Res. Lett.* 19, 034037. <https://doi.org/10.1088/1748-9326/ad281d>.
- Deline, P., Akçar, N., Ivy-Ochs, S., Kubik, P.W., 2015. Repeated Holocene rock avalanches onto the Brenva Glacier, Mont Blanc massif, Italy: a chronology. *Quat. Sci. Rev.* 126, 186–200. <https://doi.org/10.1016/j.quascirev.2015.09.004>.
- Dunai, T.J., 2010. *Cosmogenic Nuclides: Principles, Concepts and Applications in the Earth Surface Sciences*. Cambridge University Press. ed. Cambridge University Press.
- Dunning, S.A., Rosser, N.J., McColl, S.T., Reznichenko, N.V., 2015. Rapid sequestration of rock avalanche deposits within glaciers. *Nat. Commun.* 6, 7964. <https://doi.org/10.1038/ncomms8964>.
- Dussauge, C., Grasso, J., Helmstetter, A., 2003. Statistical analysis of rockfall volume distributions: implications for rockfall dynamics. *J. Geophys. Res.* 108, 2001JB000650. <https://doi.org/10.1029/2001JB000650>.
- Forbes, J.D., 1843. *Travels Through the Alps of Savoy and Other Parts of the Pennine Chain With Observations On the Phenomena of Glaciers*. Edinburgh, A. and C. Black.
- Gallach, X., Carcaillet, J., Ravanel, L., Deline, P., Ogier, C., Rossi, M., Malet, E., Garcia-Sellés, D., 2020. Climatic and structural controls on Late-glacial and Holocene rockfall occurrence in high-elevated rock walls of the Mont Blanc massif (Western Alps). *Earth Surf. Processes Landf.* 45, 3071–3091. <https://doi.org/10.1002/esp.4952>.

- Glacioclim, 2023. Service d'Observation GLACIOCLIM – Mer de Glace. <https://glacioclim.osug.fr/Mer-de-Glace>.
- Gobiet, A., Kotlarski, S., Beniston, M., Heinrich, G., Rajczak, J., Stoffel, M., 2014. 21st century climate change in the European Alps—a review. *Sci. Total Environ.* 493, 1138–1151. <https://doi.org/10.1016/j.scitotenv.2013.07.050>.
- Godon, C., Mugnier, J.L., Fallourd, R., Paquette, J.L., Pohl, A., Buoncristiani, J.F., 2013. The Bossons glacier protects Europe's summit from erosion. *Earth Planet. Sci. Lett.* 375, 135–147. <https://doi.org/10.1016/j.epsl.2013.05.018>.
- Graber, A., Santi, P., 2022. Power law models for rockfall frequency-magnitude distributions: review and identification of factors that influence the scaling exponent. *Geomorphology* 418, 108463. <https://doi.org/10.1016/j.geomorph.2022.108463>.
- Gruber, S., Haeblerli, W., 2007. Permafrost in steep bedrock slopes and its temperature-related destabilization following climate change. *J. Geophys. Res.* 112, 2006JF000547. <https://doi.org/10.1029/2006JF000547>.
- Guerin, A., Ravel, L., Matasci, B., Jaboyedoff, M., Deline, P., 2020. The three-stage rock failure dynamics of the Drus (Mont Blanc massif, France) since the June 2005 large event. *Sci. Rep.* 10, 17330. <https://doi.org/10.1038/s41598-020-74162-1>.
- Guillon, H., Mugnier, J.-L., Buoncristiani, J.-F., Carcaillet, J., Godon, C., Prud'Homme, C., Van der Beek, P., Vassallo, R., 2015. Improved discrimination of subglacial and periglacial erosion using ¹⁰Be concentration measurements insubglacial and supraglacial sediment load of the Bossons glacier (Mont Blanc massif, France). *Earth. Surf. Process. Landf.* 40 (9), 1202–1215.
- Guthrie, R.H., Evans, S.G., 2004. Magnitude and frequency of landslides triggered by a storm event, Loughborough Inlet, British Columbia. *Nat. Hazards Earth Syst. Sci.* 4, 475–483. <https://doi.org/10.5194/nhess-4-475-2004>.
- Haeblerli, W., Beniston, M., 1998. Climate change and its impacts on glaciers and permafrost in the Alps. *Ambio: J. Human Environ.* 27, 258–265.
- Haeblerli, W., Huggel, C., Kääb, A., Zraggen-Oswald, S., Polkvoj, A., Galushkin, I., Zotikov, I., Osokin, N., 2004. The Kolka-Karmadon rock/ice slide of 20 September 2002: an extraordinary event of historical dimensions in North Ossetia, Russian Caucasus. *J. Glaciol.* 50, 533–546. <https://doi.org/10.3189/172756504781829710>.
- Hantz, D., Dussauge-Peisser, C., Jeannin, M., Vengeon, J.-M., 2003. Rock fall hazard assessment: from qualitative to quantitative failure probability. *Fast Slope Movements* 263–267.
- Hantz, D., Corominas, J., Crosta, G.B., Jaboyedoff, M., 2021. Definitions and concepts for quantitative rockfall hazard and risk analysis. *Geosciences (Basel)* 11, 158. <https://doi.org/10.3390/geosciences11040158>.
- Hartmeyer, I., Delleske, R., Keuschning, M., Krautblatter, M., Lang, A., Schrott, L., Otto, J.-C., 2020. Current glacier recession causes significant rockfall increase: the immediate paraglacial response of deglaciating cirque walls. *Earth Surf. Dynam.* 8, 729–751. <https://doi.org/10.5194/esurf-8-729-2020>.
- Heisinger, B., Niedermayer, M., Hartmann, F.J., Korschinek, G., Nolte, E., Morteani, G., Neumaier, S., Petitjean, C., Kubik, P., Synal, A., Ivy-Ochs, S., 1997. In-situ production of radionuclides at great depths. *Nucl. Instrum. Methods Phys. Res. Section B* 123, 341–346. [https://doi.org/10.1016/S0168-583X\(96\)00702-1](https://doi.org/10.1016/S0168-583X(96)00702-1).
- Kargel, J.S., G.J. Leonard, M.P. Bishop, A. Kaab, B. Raup (Eds), 2014. Global land ice measurements from space (Springer-Praxis). 33 chapters, 876 pages. ISBN: 978-3-540-79817-0.
- Kaushik, S., Ravel, L., Magnin, F., Trouvé, E., Yan, Y., 2022. Ice Aprons in the Mont Blanc Massif (Western European Alps): topographic characteristics and relations with glaciers and other types of perennial surface ice features. *Remote Sens. (Basel)* 14, 5557. <https://doi.org/10.3390/rs14215557>.
- Kirkbride, M.P., Deline, P., 2013. The formation of supraglacial debris covers by primary dispersal from transverse englacial debris bands. *Earth Surf. Processes Landf.* 38, 1779–1792. <https://doi.org/10.1002/esp.3416>.
- Krautblatter, M., Funk, D., Günzel, F.K., 2013. Why permafrost rocks become unstable: a rock-ice-mechanical model in time and space. *Earth Surf. Processes Landf.* 38, 876–887. <https://doi.org/10.1002/esp.3374>.
- Le Roy, M., Nicolussi, K., Deline, P., Astrade, L., Edouard, J.-L., Miramont, C., Arnaud, F., 2015. Calendar-dated glacier variations in the western European Alps during the Neoglacial: the Mer de Glace record, Mont Blanc massif. *Quat. Sci. Rev.* 108, 1–22. <https://doi.org/10.1016/j.quascirev.2014.10.033>.
- Legay, A., Magnin, F., Ravel, L., 2021. Rock temperature prior to failure: analysis of 209 rockfall events in the Mont Blanc massif (Western European Alps). *Permafrost Periglacial* 32, 520–536. <https://doi.org/10.1002/ppp.2110>.
- Lliboutry, L., Reynaud, D., 1981. Global dynamics of a temperate valley glacier, Mer de Glace, and past velocities deduced from Forbes' bands. *J. Glaciol.* 27 (96), 207–226. <https://doi.org/10.3189/S0022143000015367>.
- Magnin, F., Josnin, J.-Y., Ravel, L., Pergaud, J., Pohl, B., Deline, P., 2017. Modelling rock wall permafrost degradation in the Mont Blanc massif from the LIA to the end of the 21st century. *Cryosphere* 11, 1813–1834. <https://doi.org/10.5194/tc-11-1813-2017>.
- Malamud, B.D., Turcotte, D.L., 2006. An inverse cascade explanation for the power-law frequency-area statistics of earthquakes, landslides and wildfires. *Geol. Soc. Lond. Spec. Publ.* 261, 1–9. <https://doi.org/10.1144/GSL.SP.2006.261.01.01>.
- Mavrouli, O., Corominas, J., 2020. Evaluation of maximum rockfall dimensions based on probabilistic assessment of the penetration of the sliding planes into the slope. *Rock Mech. Rock Eng.* 53, 2301–2312. <https://doi.org/10.1007/s00603-020-02060-z>.
- Millan, R., Mougnot, J., Rabatel, A., Morlighem, M., 2022. Ice velocity and thickness of the world's glaciers. *Nat. Geosci.* 15, 124–129. <https://doi.org/10.1038/s41561-021-00885-z>.
- Orr, E.N., Owen, L.A., Saha, S., Hammer, S.J., Caffee, M.W., 2021. Rockwall slope erosion in the northwestern Himalaya. *JGR Earth Surface* 126, e2020JF005619. <https://doi.org/10.1029/2020JF005619>.
- Peyaud, V., Bouchayer, C., Gagliardini, O., Vincent, C., Gillet-Chaulet, F., Six, D., Laarman, O., 2020. *Cryosphere* 14, 3979–3994.
- Puchol, N., Lavé, J., Lupker, M., Blard, P.H., Gallo, F., France-Lanord, C., Team, A.S.T.E.R., 2014. Grain-size dependent concentration of cosmogenic ¹⁰Be and erosion dynamics in a landslide-dominated Himalayan watershed. *Geomorphology* 224, 55–68. <https://doi.org/10.1016/j.geomorph.2014.06.019>.
- Rabatel, A., Deline, P., Jaillet, S., Ravel, L., 2008. Rock falls in high-alpine rock walls quantified by terrestrial lidar measurements: a case study in the Mont Blanc area. *Geophys. Res. Lett.* 35, L10502. <https://doi.org/10.1029/2008GL033424>.
- Rabatel, A., Ducasse, E., Millan, R., Mougnot, J., 2023. Satellite-derived annual glacier surface flow velocity products for the European Alps, 2015–2021. *Data* 8, 66. <https://doi.org/10.3390/data8040066>.
- Ravel, L., Deline, P., 2008. La face ouest des Drus (massif du Mont-Blanc) : évolution de l'instabilité d'une paroi rocheuse dans la haute montagne alpine depuis la fin du petit âge glaciaire. *Géomorphologie* 14, 261–272. <https://doi.org/10.4000/geomorphologie.7444>.
- Ravel, L., Allignol, F., Deline, P., Gruber, S., Ravello, M., 2010. Rock falls in the Mont Blanc Massif in 2007 and 2008. *Landslides* 7, 493–501. <https://doi.org/10.1007/s10346-010-0206-z>.
- Ravel, L., Deline, P., Jaillet, S., 2011. Four years of monitoring of rockwall morphodynamics in the Mont-Blanc massif by terrestrial laserscanning. *Collection EDYTEM* 12, 69–76 b.
- Ravel, L., Deline, P., 2013. A network of observers in the Mont-Blanc massif to study rockfall from high Alpine rockwalls. *Geografia Fisica e Dinamica Quaternaria* 36, 151–158. <https://doi.org/10.4461/GFQD.2013.36.12>.
- Ravel, L., Magnin, F., Deline, P., 2017. Impacts of the 2003 and 2015 summer heatwaves on permafrost-affected rock-walls in the Mont Blanc massif. *Sci. Total Environ.* 609, 132–143. <https://doi.org/10.1016/j.scitotenv.2017.07.055>.
- Robock, A., 1979. Little ice age: northern hemisphere average observations and model calculations. *Science (1979)* 206, 1402–1404.
- Ruiz-Carulla, R., Corominas, J., Mavrouli, O., 2017. A fractal fragmentation model for rockfalls. *Landslides* 14, 875–889. <https://doi.org/10.1007/s10346-016-0773-8>.
- Sarr, A.-C., Mugnier, J.-L., Abrahami, R., Carcaillet, J., Ravel, L., 2019. Sidewall erosion: insights from *in situ* -produced ¹⁰Be concentrations measured on supraglacial clasts (Mont Blanc massif, France). *Earth Surf. Processes Landf.* 44, 1930–1944. <https://doi.org/10.1002/esp.4620>.
- Scherler, D., Egholm, D.L., 2020. Production and transport of supraglacial debris: insights from cosmogenic ¹⁰be and numerical modeling, Chhota Shigri Glacier, Indian Himalaya. *JGR Earth Surface* 125, e2020JF005586. <https://doi.org/10.1029/2020JF005586>.
- Schovanec, H., Walton, G., Kromer, R., Malsam, A., 2021. Development of improved semi-automated processing algorithms for the creation of rockfall databases. *Remote Sens. (Basel)* 13, 1479. <https://doi.org/10.3390/rs13081479>.
- Six, D., Vincent, C., 2014. Sensitivity of mass balance and equilibrium-line altitude to climate change in the French Alps. *J. Glaciol.* 60, 867–878. <https://doi.org/10.3189/2014JoG14J014>.
- Teledyne Geospatial Optech, 2024. ILRIS-LR Terrestrial Laser Scanner. Summary specification sheet. <https://pdf.directindustry.com/pdf/optech/ilris-lr/25132-387459.html>.
- Turcotte, D.L., 1986. Fractals and fragmentation. *J. Geophys. Res.* 91, 1921–1926. <https://doi.org/10.1029/JB091iB02p01921>.
- Vallot, J., 1900. Expériences sur la marche et la variation de la Mer de Glace (in French). *Annales de l'Observatoire Météorologique* 4, 35–157. *Physique et Glaciaire du Mont-Blanc*.
- Vincent, C., 2002. Influence of climate change over the 20th Century on four French glacier mass balances. *J. Geophys. Res.* 107. <https://doi.org/10.1029/2001JD000832>.
- Vincent, C., Fischer, A., Mayer, C., Bauder, A., Galos, S.P., Funk, M., Thibert, E., Six, D., Braun, L., Huss, M., 2017. Common climatic signal from glaciers in the European Alps over the last 50 years. *Geophys. Res. Lett.* 44, 1376–1383. <https://doi.org/10.1002/2016GL072094>.
- von Blanckenburg, F., 2006. The control mechanisms of erosion and weathering at basin scale from cosmogenic nuclides in river sediment. *Earth Planet. Sci. Lett.* 242, 224–239. <https://doi.org/10.1016/j.epsl.2005.06.030>.
- Ward, D.J., Anderson, R.S., 2011. The use of ablation-dominated medial moraines as samplers for ¹⁰Be-derived erosion rates of glacier valley walls, Kichatna Mountains, AK. *Earth Surf. Processes Landf.* 36, 495–512. <https://doi.org/10.1002/esp.2068>.
- Wetterauer, K., Scherler, D., Anderson, L.S., Wittmann, H., 2022. Temporal evolution of headwall erosion rates derived from cosmogenic nuclide concentrations in the medial moraines of Glacier d'Otemma, Switzerland. *Earth Surf. Processes Landf.* 47, 2437–2454. <https://doi.org/10.1002/esp.5386>.
- Wetterauer, K., Scherler, D., 2023. Spatial and temporal variations in rockwall erosion rates derived from cosmogenic ¹⁰Be in medial moraines at five valley glaciers around Pigne d'Arolla, Switzerland. *Earth Surf. Dynam.* 11, 1013–1033. <https://doi.org/10.5194/esurf-11-1013-2023>.